EXPERIMENTS ON TUNED UHBR OPEN-TEST-CASE FAN ECL5/CATANA: PERFORMANCE AND AERODYNAMICS

Alexandra Patrizia Schneider, Anne-Lise Fiquet, Benoit Paoletti, Xavier Ottavy, Christoph Brandstetter

PREPRINT: EXPERIMENTS ON TUNED UHBR OPEN-TEST-CASE FAN ECL5/CATANA: PERFORMANCE AND AERODYNAMICS

Alexandra P. Schneider, Anne-Lise Fiquet, Benoit Paoletti, Xavier Ottavy and Christoph Brandstetter*

Université de Lyon, École Centrale de Lyon, CNRS, LMFA, UMR 5509, F-69134, ECULLY, France

ABSTRACT

With the advancement of modern fan architectures the lack of experimental benchmarks for the research community became apparent in the recent years. Enormous effort in method development could not be validated on representative geometries and motivated the development of the open-test-case ECL5/CATANA. A carbon fibre fan stage has been designed by Ecole Centrale de Lyon and shared with the community in 2021. The fan is representative of a modern Ultra High Bypass Ratio (UHBR) architecture with sonic design speed. The reference configuration has been investigated experimentally on a novel test facility with multi-physical instrumentation. In this publication the results of the first experimental campaign are presented with a detailed analysis of the aerodynamic performance and system symmetry. The presented results comprise full stage mappings across the whole operating range for three main speedlines (55%, 80% and 100%) using performance rakes, unsteady wall-pressure arrays, tip-clearance and stagger-angle measurements. Radial profiles of intake boundary layer and rotor-exit conditions at selected conditions complete the full validation dataset for steady and unsteady aerodynamic simulations. Results are discussed in comparison to blind-test RANS simulations of different international institutes. Significant predicition inaccuracies of the tip flow and corner separations of the stator are observed and reveal the requirement of real-blade-geometry measurements at running conditions. This paper is accompanied by a publication with a focus on aeroelastic instabilities observed near the stability limit. The results represent a comprehensive dimensional benchmark dataset and allow method validation on multiple levels of fidelity for the aerodynamic and aeroelastic research community.

NOMENCLATURE

Abbreviations

DP	Design Point
ECL	Ecole Centrale de Lyon
FEM	Finite Element Method
NC	Near Choke
NS	Near Stall
NSV	Non-synchronous vibrations
PE	Peak Efficiency
PP	Peak Pressure
RMS	Root Mean Square
TLF	Tip Leakage Flow
(U)HBR	(Ultra) High Bypass Ratio
(U)RANS	(Unsteady) Reynolds Averaged Navier-Stokes

Greek letters

α	circumferential flow angle [°]
γ	heat capacity ratio [-]
Π	pressure ratio [-]
η	efficiency [-]

Roman letters

c	axial chord [mm]
c_p	specific heat capacity [$Jkg^{-1}K^{-1}$]
$\dot{m}$	massflow rate [kgs^{-1}]
p	pressure [Pa]
P_{mec}	mechanical power [W]
T	temperature [K]

Dimensionless groups

M	Mach number, u/c

Superscripts and subscripts

s	static
t	total

Introduction

Latest design trends in turbomachinery, especially concerning the geared turbofan, result in fan geometries with lightweight, 3D-shaped rotor blades with reduced tip Mach number. Compared to existing reference configurations like the NASA rotors 37, 67 or the TU Darmstadt Rotor 1, which are metallic high-speed designs, substantial changes of stable operating range limiting phenomena are observed: higher susceptibility to blade vibration, reduced flutter frequencies, altered acoustic interaction due to shorter intake lengths [1], higher sensitivity to geometric asymmetry due to reduced shock strength and solidity [2] and strongly non-linear fluid-structure-interaction at low-frequencies related to pressure untwist of the blades [3]. Existing design criteria are not suitable to capture these coupled

preprint/accepted manuscript: A. P. Schneider, A-L. Fiquet, B. Paoletti, X. Ottavy and C. Brandstetter*, "Experiments on tuned UHBR open-test-case Fan ECL5/CATANA: Performance and aerodynamics." ASME Turbo Expo 2023.
*corresponding author christoph.brandstetter@ec-lyon.fr

aerodynamic, structural and acoustic phenomena of modern architectures.

The combination of advanced numerical methods and experiments at representative conditions is required to enhance the understanding of complex multi-physical interactions, validate and improve design methods that are required to advance technology. To overcome the gap of available configurations representative for low-speed Ultra High Bypass Ratio (UHBR) designs, the open-test-case composite fan ECL5 has been developed at Ecole Centrale de Lyon (ECL). Geometry and structural properties have been shared with the research community [4] and are already used by international research institutes. In project CATANA (catana.ec-lyon.fr) numerical and experimental studies are conducted and here we present the first experimental results of the reference configuration.

The design of the stage was based on three objectives which are aligned with industrial requirements for near future configurations concerning maximum efficiency and pressure ratio at design conditions, specific massflow density, over-speed capability and sufficient operating range across all speedlines. Industrial practices to minimize the risk of flutter have been applied, which is in contrast to the complementary research program CA3VIAR [5]. The detailed design process was presented in [6, 7]. It resulted in a 16-bladed carbon-fibre composite configuration with a relative design tip Mach number of 1.02 at a tip speed of 288 m/s, which is significantly lower than state-of-the-art industrial UHBR configurations like the direct drive LEAP or GEnx, but also compared to the only in-service geared turbofan PW1000, promising extensive potential for noise reduction and improvement of propulsive efficiency. Numerical pre-studies at design speed have predicted enormous aerodynamic potential of a stage peak isentropic efficiency above 92% at a mass-flow rate of 36 kg/s but also a wide range between 32 kg/s and 39 kg/s in which efficiency does not drop below 88%.
However, unsteady simulations indicated the potential risk of non-synchronous vibrations (NSV) at 80% speed due to convective aerodynamic disturbances [8], a phenomenon that is known for high-pressure compressors [9, 10]. It has only recently been described to occur in low-speed composite fans [11, 12], also revealing a significant influence of turbulence-modeling on the accuracy of performance prediction, highlighting the shortcomings of established numerical methods.

These studies indicated that significant knowledge gaps persist today and prediction of performance and instability is challenging. The goal of the study presented here is to provide a benchmark dataset on a geometry that is representative of near future architectures that allows detailed validation and calibration of prediction methods on multiple levels of fidelity for the whole research community. This ranges from reduced order models as described by [13,14] to scale resolving coupled methods which are on the verge of being accessible to this type of architecture [15, 16, 17, 18, 19].

The fan stage is experimentally investigated on the facility ECL-B3 [20], which provides extensive steady and unsteady instrumentation for aerodynamics, acoustics and structure dynamics. In this study, a structurally tuned rotor configuration is investigated at different speedlines and operating conditions, ranging from choke to near-stall.

The objectives of the presented study aim to respond to the main aerodynamic and aeroelastic questions associated with the composite fan design:

· low hub-to-tip ratio designs with wide midspan chord result in high turning angles near the hub and non-uniform pressure profiles, which are challenging for simulations. Radial flow migration occurs and influences the aeroelastic behaviour [21]. For the ECL5 design, predictions were ambiguous [7, 8] and vary dependent on the used method. The main objective is to clearly characterize the aerodynamic flow field and instability mechanism across the whole speed range.
· Torsionally flexible blades such as designed for ECL5 require more tip clearance to ensure safe operation than conventional designs: Significant endwall-blockage due to tip-leakage flow is hence expected, which is relevant for NSV but also challenging for numerical methods. Furthermore, sensitivity to non-linear aerodynamics that cause alternating stagger patterns and non-symmetric running geometry is expected [3, 2]. The study presented here aims to resolve the real running geometry and aerodynamics to provide a comprehensive benchmark dataset.

In this publication the open-test-case and the experimental setup is introduced before we present the complete baseline for aerodynamic simulations: Performance measurements, radial pneumatic probe profiles downstream of the fan, a description of the operability range and turbulent inflow conditions. Particular focus is laid on the evolution of circumferential asymmetry, which has been identified as a characteristic issue for low-transonic composite fans. Using different methods, the unintended asymmetry of blade stagger and tip clearance is measured and correlations with the local aerodynamic field are discussed.

This represents a novelty for the community, as it allows for in-depth validation of numerical methods on a modern geometry.

A detailed analysis of the onset of instability at different operating speeds with a focus on aeroelastic interaction is presented in the accompanying paper [22].

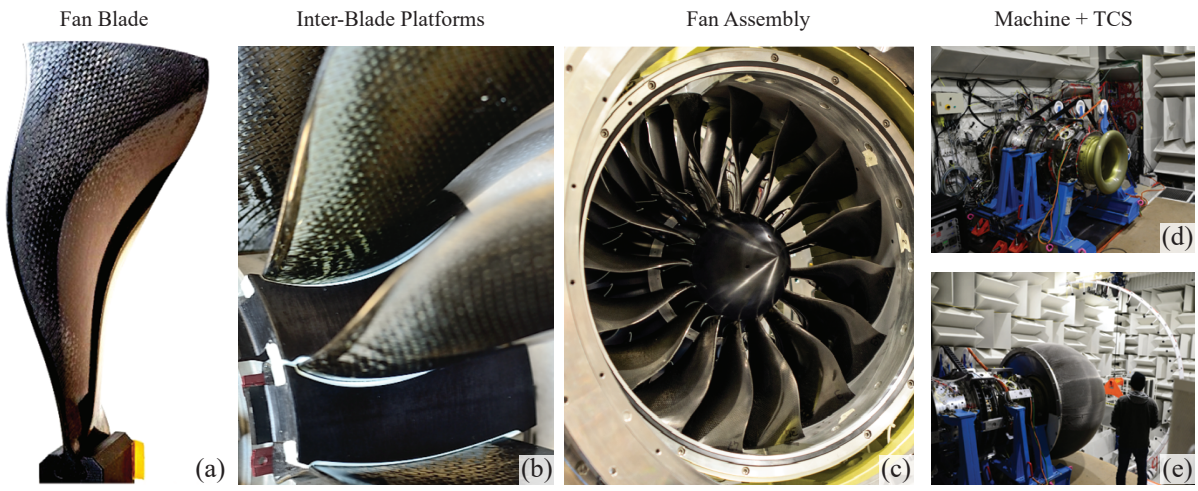

FIGURE 1: Rotor blades, rotor assembly and facility

1 Experimental Setup

1.1 The Open-Test-Case Fan stage

As summarized above, research of the past decades has shown that aeroelastic instability mechanisms of typical machines from the late 20th century are not similar to those observed in modern compressors and low-pressure ratio fans.

To provide a representative test case that produces relevant aerodynamic features, acoustic signatures and aeroelastic instability mechanisms, industrial objectives on pressure-ratio, massflow density and operability range have been employed and detailed in [6] with substantial support from Safran Aircraft Engines. A low-transonic, 16-bladed carbon fibre design was developed with a predicted pressure ratio of 1.35 at design conditions, a wide range of high isentropic efficiency and 5% transonic over-speed capability.

Structurally, the first three fan-blade eigenmodes were designed according to industrial practices by varying the carbon fibre orientations. Fan blades have been fabricated from pre-impregnated layers, which are cut, oriented and stacked according to the layup described in [7] and shown in Fig. 1(a). Each fabricated blade was 3D-scanned, the frequency response, static moment and mass determined, and selected blades were used for tomography analysis to investigate air-inclusions. Based on these studies, two configurations were selected, the first reference configuration with maximum frequency tuning, presented in this publication, and a second mistuned configuration which will be investigated in the future. Details on the tuning of the reference configurations are given in [22]. The blades are assembled on a titanium disk and inter-blade platforms are integrated with silicon-joints as presented in Fig. 1(b).

The OGV consists of 31 conventionally manufactured aluminium vanes, located far downstream of fan to minimize interactions with the rotor. As the facility provides no bypass flow channel, engine representative stator aerodynamics are not intended, but axial stage outflow and homogeneous radial conditions have to be ensured to allow detailed performance analysis.

Key parameters of the design process are summarized in Tab. 4.

1.2 Test facility, instrumentation and experimental procedures

The experiments were performed at the test facility ECL-B3 at Ecole Centrale de Lyon, shown in Fig. 1. The rig was built in cooperation between ECL and Safran Aircraft Engines through the ANR- EQUIPEX program for aerodynamic, aeroelastic and acoustic investigation of fans at scales around 1:4.

The core section of the rig with the fan stage Fig. 1(d) is placed in an anechoic chamber Fig. 1(e), acoustically isolated from the machine room hosting a 3 MW electric motor. A gearbox between motor and rotor shaft enables rotational speeds up to 16000 rpm. The rig is operated in an open cycle. Air enters the anechoic chamber from the roof and is sucked into the core section. Downstream of the core section an axisymmetric throttle is used to control massflow rate. A detailed description of the facility is presented in [20].
A turbulence control screen (TCS) Fig. 1(e) is installed in front of the machine core to ensure homogeneous inflow conditions and reduce large scale turbulence [12].

Figure 2 presents an overview of the core instrumentation in different measurement planes, the global coordinate system and the intake geometry. In the machine intake (in), two combined total pressure and temperature rakes are integrated for performance measurements, together with two traversable rakes downstream of the stage (SE). Humidity and atmospheric conditions are measured in the chamber.

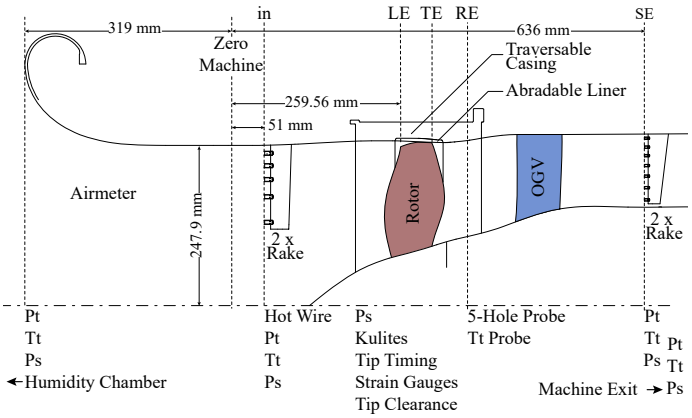

FIGURE 2: Schematic view of machine core and probe positions

The massflow rate $\dot{m}_{std}$ through the fan stage is determined based on static pressure $p_{s,in}$, total pressure $p_{t,in}$ and total temperature $T_{t,in}$ in the stage intake and corrected to international standard atmosphere (ISA) conditions.

When rakes in the stage intake are present, $p_{t,in}$ and $T_{t,in}$ are derived by mass averaging values from different radial measurement positions indicated by $\overline{\overline{(\cdot)}}$. Gas-constants are corrected for humidity.

To obtain the stage exit plane (Fig. 3), two rakes separated by 180° are traversed around the machine axis at stable operating conditions (black dots in Fig. 3). Static pressure is measured at hub and casing and assumed to evolve linearly over the channel height to enable for mass-weighted averaging of the presented fan stage characteristics, i.e. total pressure ratio

$$\Pi_{t,stage} = \frac{\overline{\overline{p}}_{t,SE}}{\overline{\overline{p}}_{t,in}} \tag{1}$$

and stage efficiency η_{stage} based on shaft power P_{mec}

$$\eta_{stage} = c_p T_{t,0} \dot{m} \frac{\left(\Pi_{t,stage}\right)^{\frac{\gamma-1}{\gamma}} - 1}{P_{mec}} \tag{2}$$

5-hole probe and total temperature measurements (miniature probes from Limmat Scientific) at selected operating points are used to determine radial profiles of total pressure ratio, flow angle and total temperature between rotor and stator.

Unsteady instrumentation in several axial and circumferential positions is used to resolve machine and rotor aerodynamics as well as the aeroelastic behavior. Fast-response wall pressure transducers (WPT, Kulite XCS-062) in multiple axial and circumferential positions allow detailed analysis of rotor tip aerodynamics, shock structure at transonic operating conditions, circumferential flow inhomogeneities and the convective aerodynamic disturbances and stall onset. Blade vibration is primarily monitored with a capacitive system with sensors, acquisition and evaluation provided by MTU, conditioners by Fogale. Furthermore, blade-mounted strain gauges are applied on each rotor blade as well as on one of three OGV blades and continuously online monitored.

Boundary layer in the stage intake and inflow turbulence are measured using hot wire probes (TSI 1212-T1.5 in CTA configuration, DANTEC Streamline conditioner) which are traversed in radial direction at stable operating conditions. Hot wires have been calibrated for varying Mach number and temperature. A Cox based correction [23] has been applied in the region very close to the casing to take heat transfer into account.

1.3 Numerical Simulations

The experimental results are compared to Reynolds-Averaged Navier-Stokes (RANS) simulations conducted at ECL during the design process. A structured mesh of a single passage has been created using AutoGrid5 with $4.4x10^6$ points, comparable to the mesh used in [24]. The wall resolution of this mesh is below $y^+ = 1$ for design conditions which corresponds to a massflow rate of $\dot{m}_{std} = 36$ kg/s at design speed. The flow solver is elsA, an unsteady RANS solver developed by ONERA [25]. The Jameson scheme is used with second-order accuracy in space, as well as the $k-\omega$ Kok model to calculate turbulence, no transition model was applied. For steady simulations, total pressure, total enthalpy and flow angles are specified at the intake. Static-pressure condition and radial equilibrium with quadradic valve-law is applied at the exit. For all steady calculations presented within this study a mixing-plane has been used to model the interface between stationary and rotating domain.

2 Aerodynamic Performance

To measure aerodynamic performance of the stage, rakes are installed in the intake and downstream of the OGV (Fig. 2). After a full acceleration run to 105% speed (N105) the machine was stabilized at respective speedlines, corrected to ISA conditions. Starting at fully-open conditions, operating points were thermically stabilized and rake traverses recorded with 15 circumferential points per OGV passage.

Figure 3(a) shows the measured exit-plane total pressure for two different operating points at design speed N100, compared to RANS simulations at the numerical design point (DP) and the point of maximum total pressure ratio (peak pressure, PP). Each presented contour map has been normalized with the mass-averaged total pressure ratio (as shown in Fig. 4(a)) of the respective operating point.

For both operating conditions a clear stator wake is visible from about 25% to 82% channel height. Close to the hub and the casing, regions of reduced pressure ratio compared to mid channel values indicate corner separation [26].

The comparison of both operating points shows that reducing the massflow rate from DP to PP, hence slightly increasing the

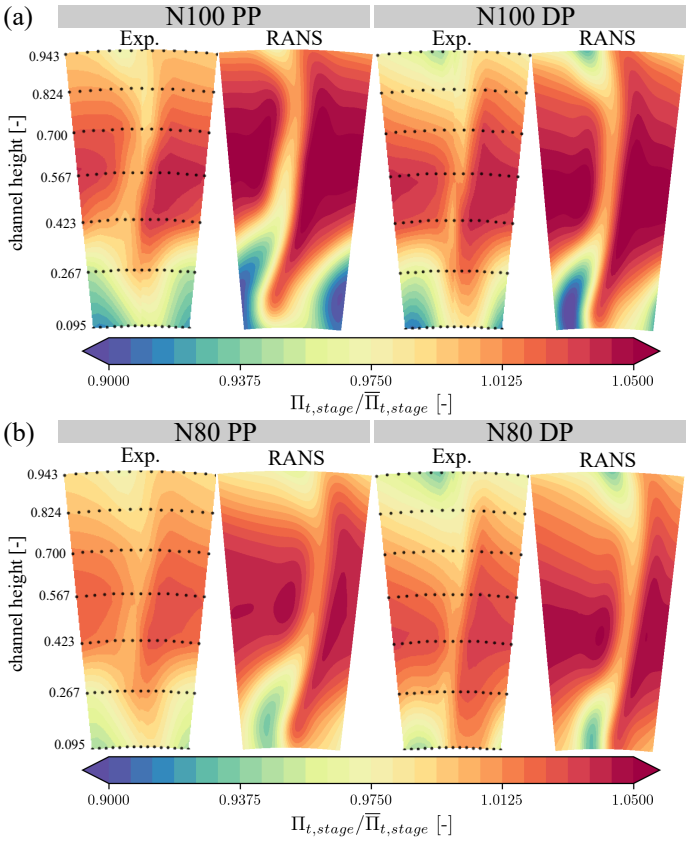

FIGURE 3: Total pressure contour from rake traverse at stage exit (SE) normalized with mass-averaged stage total pressure ratio and comparison to RANS simulations

achieved stage total pressure ratio (compare Fig. 4), is accompanied by a minor change of the corner separation. The stator wake at midspan is significantly more intense at PP condition.

Steady RANS results shown in Fig. 3(a) have been interpolated to the same grid as the experimental data and values in the vicinity of hub and casing have been excluded to improve comparability. For both operating conditions the numerical flow field shows a higher normalized total pressure ratio at medium channel heights while the pressure ratio in the stator wake is comparable to the experimental values. Hence, numerically computed pressure gradients between passage flow and stator wake are higher compared to experimental results. For both massflow rates RANS simulations over-estimate intensity and radial extend of the corner separation at the hub. The pressure drop in the separation zone exceeds 10% in numerical simulations while it is about 8-9% in experiments with respect to the mass-averaged value. Both experimental and numerical results show a slightly reduced pressure deficit at the OGV hub as the massflow is decreased from DP to PP, accompanied by an increase of radial and circumferential extend of the separation zone due to an increased incidence [27].

Close to the casing i.e. in the upper 15% of the channel, experimentally observed pressure ratio is lower compared to numerical results.

To analyze observed differences at part speed, Fig. 3(b) compares RANS simulation and experiment at 80% design speed (N80) for the respective PP and DP operating points. As before, RANS simulation shows higher normalized total pressure ratio at midspan and a clearly defined stator wake. The corner separation at the OGV hub as well as total pressure ratio close to the casing are again over-estimated confirming the observations for design speed.

It has to be considered, that the experiment uses Kiel-heads on the rakes of diameter 3 mm and hence appears spatially filtered, but the extent of the corner separation and differences between experiment and CFD exceed the associated effect. According to literature, this over-estimation can be associated to the applied turbulence model. Underlying assumptions such as steady flow, isotropic turbulence and local equilibrium of turbulence production and destruction are not fulfilled in the region of the corner separation where multi-scale vortical structures are present. Hence, classical turbulence models (without modifications) prevent accurate simulation of the OGV corner separation [28, 29]. The over-estimation of total pressure close to the casing is associated to a systematic shortcoming of the the numerical setup as well. The mixing plane applied at the rotor-OGV interface prevents the accurate simulation of the transfer of the tip leakage vortex through the stator domain and its interaction with the casing OGV corner separation, yielding reduced losses at the stator exit compared to experimental results.

The rake traverses as presented in Fig. 3 have been performed at 55%, 80%, 90%, 100% and 105% design speed for various massflow rates at each speedline. Mass averaging measured total pressure and temperature allows to derive the fan stage characteristics i.e. total pressure ratio $\Pi_{t,stage}$ and η_{stage} as a function of standardized massflow rate $\dot{m}_{std}$, presented in Fig. 4(a) and (b). In both cases results from wall-resolved RANS simulations from the design process of the fan stage are included for comparison.

Figure 4 provides a good agreement between steady numerical and experimental fan stage characteristic for all investigated speedlines and massflow rates.

At design speed i.e. low transonic operating conditions, the achieved total pressure ratio is slightly over-estimated in simulations for nearly all massflow rates. Near peak pressure (PP) operating conditions the difference is about 0.25%, resulting from an over-estimation of achieved total pressure ratio in the midspan region (compare Fig. 3) which is not fully compensated by the over-estimated OGV-corner separation. Only the operating point at a massflow rate of $\dot{m}_{std} = 36.9\,\mathrm{kg/s}$ - corresponding to the operating point where maximum efficiency is reached in experiments - provides a slightly higher total pressure ratio than numerically computed. Therefore, the drop in total pressure ratio from the

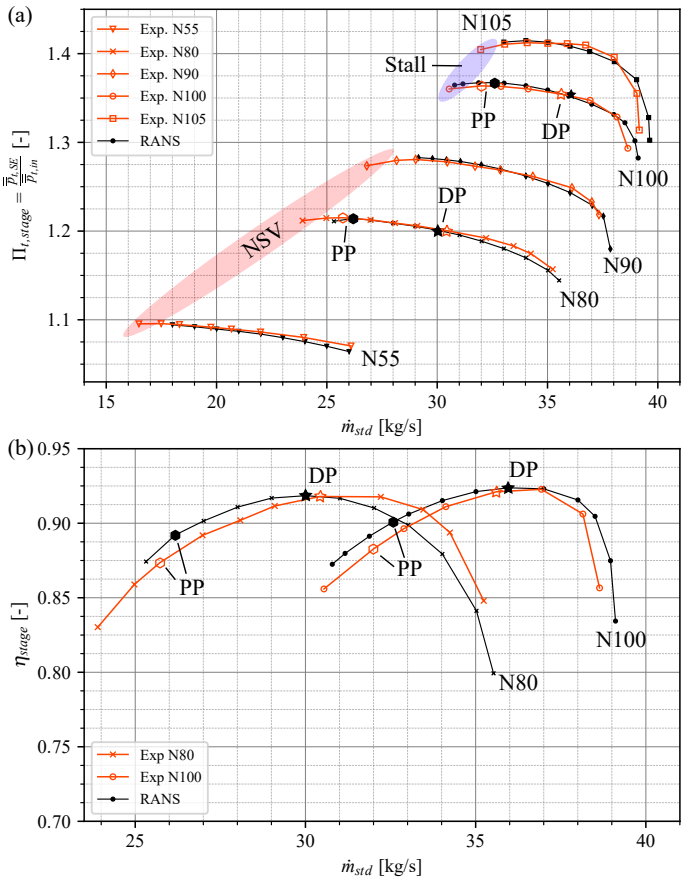

FIGURE 4: Fan stage characteristic

design point to higher massflow rates is stronger compared to the numerical data. The same trend is visible for 105% design speed, resulting in an over-estimation of choke massflow by RANS simulations for both speedlines. This is particularly interesting when considering the measured stagger angle, discussed in section 3.2.

Towards low massflow rates the stable operating range is limited by the onset of rotating stall for 100% and 105% design speed. This is in agreement to previously performed unsteady numerical simulations presented in [30], which give a good estimation of the experimentally measured stall massflow but obviously deviate from the steady RANS simulations presented here.

At part speed conditions measured total pressure ratio is slightly higher than estimated for high massflow rates (up to 0.6%, 0.44% and 0.43% at 55%, 80% and 90% design speed respectively) whereas it coincides with numerical results for lower massflow. At all subsonic speedlines, throttling the rotor towards lower massflow leads to the rise of non-synchronous vibrations and abortion of the experiment before the onset of rotating stall. Experiments have been stopped when 50% of the Goodman scope-limit were reached. The most critical blade eigenmodes differ between the speedlines, but in all cases stable limit-cycle levels at continuously increasing amplitudes were observed from the respective peak-pressure condition towards the stability limit. A detailed analysis is provided in [22].

Figure 4(b) presents stage efficiency η_{stage} for 100% and 80% design speed calculated based on mass averaged total pressure ratio in the stage exit according to Eq. 2. θ At design speed the measured maximum efficiency $\eta_{max,\mathrm{N100}} = 92.3\%$ is in good agreement with the efficiency of the numerical design point $\eta_{\mathrm{DP}} = 92.6\%$. However, peak efficiency is reached at a massflow rate of $\dot{m}_{std} = 36.9$kg/s in experiments, resulting in a slightly lower efficiency for the operating point close to the numerical design point. In experiments the drop in efficiency towards higher and lower massflow rates is stronger compared to the numerical data. Hence, stage efficiency is significantly over-estimated by RANS simulations, with up to 5% for high massflow rates and with approximately 1.5% for low massflow rates. At the 80% speedline, which is representative for all investigated part speedlines, magnitude of stage efficiency ($\eta_{max,\mathrm{N80exp}} = 91.6\%$) and curve form are in good agreement with numerical estimations ($\eta_{max,\mathrm{N80num}} = 91.8\%$). The shift in peak efficiency massflow observed for design speed is also found at part speed but concerns all massflows in this case. Here, a clear correspondence to the slightly reduced stagger angle in the experiment as discussed in section 3.2 is evident and must be considered in future simulations of the setup.

For both presented speedlines in Fig. 4(b) the numerically computed efficiency at operating point PP is higher than the experimental result, despite the over-estimated OGV-corner separation, indicating that other loss mechanisms are not fully resolved by performed RANS simulations.

The presented results from the performance measurements prove overall good agreement of numerical simulations performed within the design process of the ECL5 stage with experiments. Local deviations have been identified in regions of flow separation and strong mixing and attributed to the numerical setup.

2.1 Probe measurements

Radial profiles of 5-hole probe measurements downstream of the fan (rotor exit plane, RE) are presented in Fig. 5 for three operating points at 100% speed, near choke NC, design point DP and peak pressure PP as well as two respective operating points at 80% speed. Total pressure ratio profiles, circumferential flow angle and total temperature are compared to steady RANS simulations. For all three operating points at design speed excellent agreement is observed for the lower 60% of span. Towards the casing, experiments show a slightly lower pressure ratio between 70 and 90% span for design and peak pressure conditions, indicating inaccurate simulation of the tip flow i.e. the interaction of the tip leakage flow with the main passage flow. As already discussed above for the stator exit-flow, this is caused by the assumptions of steady flow and the turbulence model inherent to

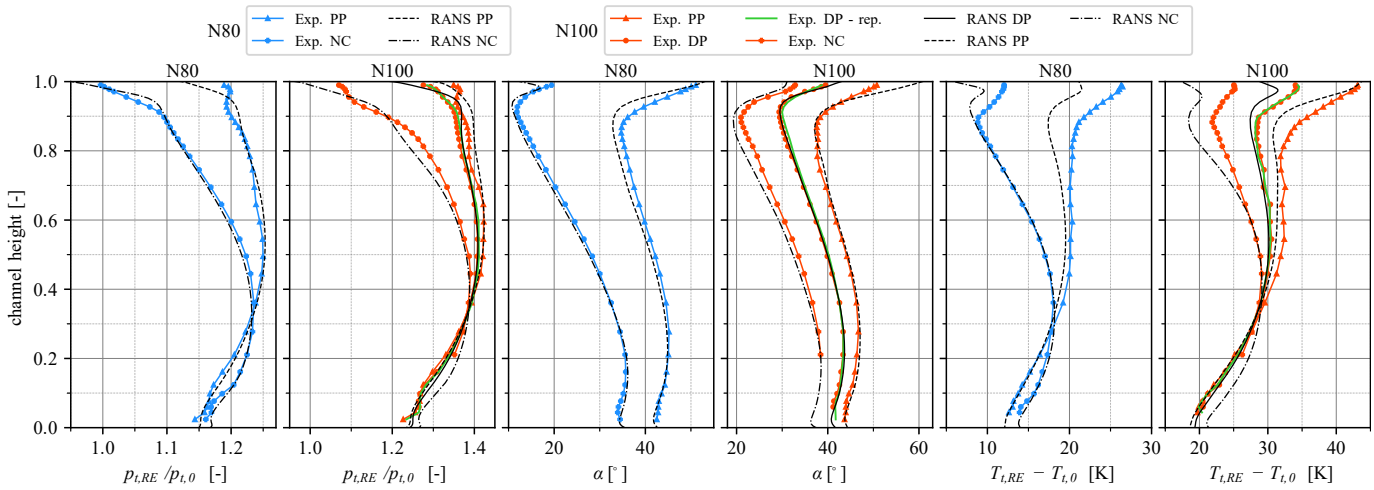

FIGURE 5: Comparison of measured and RANS based radial profiles at rotor exit (RE)

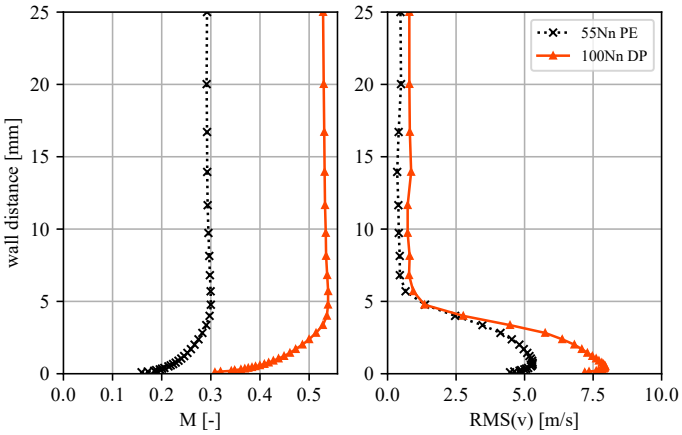

FIGURE 6: Boundary layer velocity profiles from hot wire measurements in the stage intake (IN)

the numerical setup. At near choke conditions, a slightly higher total pressure ratio is experimentally observed in this region in contrast to DP and PP. Comparing the swirl angle in Fig. 5 very close agreement between RANS and experiment is observed over the whole channel height at 100% design speed. At PP condition, the maximum deviation to CFD amounts to 10° at the casing, but at lower channel heights the difference to numerical computations is below 1° for PP and DP operating conditions, even close to the hub where numerical simulations indicate strong radial migration. The graphs show that despite a slightly increased turning angle, the fan operates at constant total pressure ratio at the hub for both operating points. For near choke conditions a slightly increased circumferential flow angle is observed in experiments, especially between 60% channel height and casing. Hence, work input of the rotor is increased compared to numerical estimations resulting in a higher total temperature rise. As total pressure ratio is nearly identical between experiments and RANS simulations, the higher temperature rise over the rotor results in decreased efficiency visible in Fig. 4(b).

To investigate repeatability of the presented measurements, selected measurements have been repeated within a time interval of one month, from which N100 DP is exemplarily presented in Fig. 5 (green line). The comparison of both design point measurements at 100% speed provides excellent repeatability despite changing atmospheric conditions.

At 80% design speed a good agreement between numerical estimation and experimental data is observed as well, notably for lower channel heights. For NC operating conditions deviations in total pressure ratio, circumferential flow angle and total temperature rise are marginal up to 90% channel height and only slightly increased towards the casing. As OGV-corner separation is strongly over-estimated by RANS simulations (see Fig. 3(b)) measured stage efficiency is significantly higher compared to numerical data at this operating point. At lower massflow rate i.e. peak pressure conditions, differences are observed in turning angle from 40% channel height increasing towards the casing. As above the increased flow angle observed in experiment results in an increased temperature rise over the rotor, thus resulting in an reduced stage efficiency compared to numerical estimations. Figure 6 presents boundary layer velocity profiles from hot wire measurements in the stage intake (in). Axial Mach number and root mean square (RMS) of axial velocity are shown for two different speedlines as a function of wall distance from the casing from 0 mm to 25 mm corresponding to approximately 10% channel height. The boundary layer profile is consistent for both operating points. The presentation of the RMS values reveals the level of turbulence. For all operating points, the main flow velocity is reached at a wall distance of 5 mm i.e. 2% channel height.

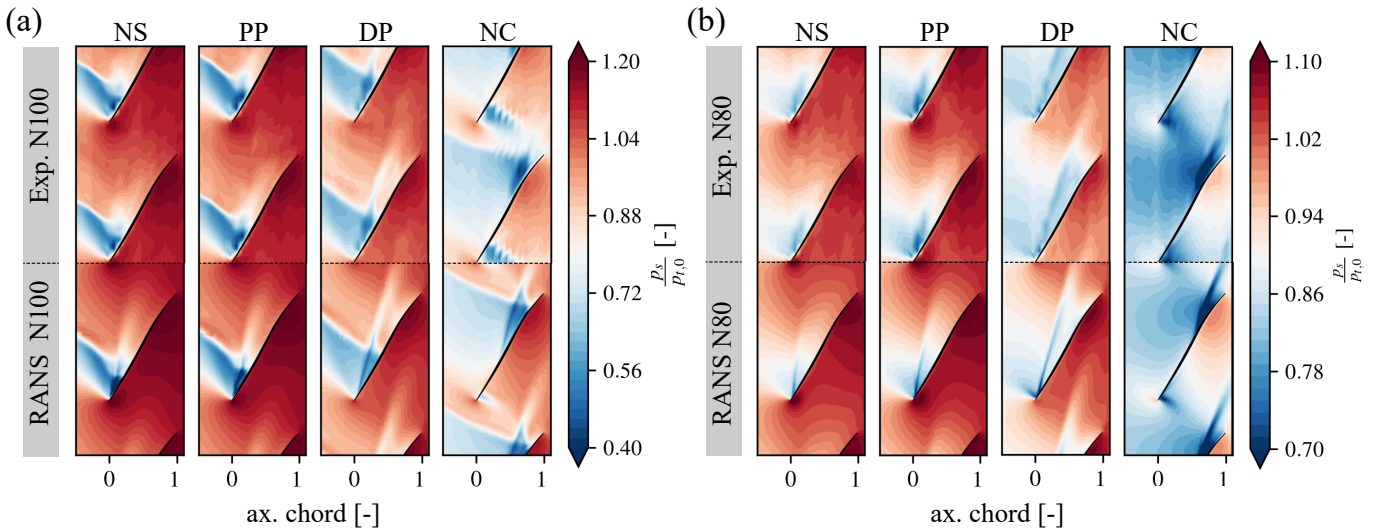

FIGURE 7: Static pressure field at rotor casing for different operating conditions

2.2 Rotor tip aerodynamics

A detailed overview of the rotor tip aerodynamics is given in Fig. 7 which shows the static pressure field for different operating conditions side by side with RANS results. The figures are obtained by ensemble averaging the signals of the axial WPT array in the rotor casing over 200 revolutions to remove temporal fluctuations. To allow a better comparison with the perfectly periodic wall pressure field from the single-passage simulations, experimental data has been additionally averaged over all 16 blade passages to exclude blade-to-blade inhomogeneity. Differences resulting from these blade-to-blade differences will be discussed in detail in the following section.

Figure 7(a) presents the comparison of static wall pressure field for different operating conditions at design speed. Transonic conditions with clearly defined shocks are visible for all operating points. Throttling the rotor from near choke (NC) to near stall (NS) shifts the shock away from the leading edge (LE). At the design point of the rotor a far detached shock is observed, which is in contrast to existing HBR-configurations running at higher relative rotational speed. Influence of tip leakage flow and its interaction with the shock is observable at all shown operating conditions.

The numerical simulation coincides well with the experimentally measured flow field. Pressure gradients from blade pressure to suction side are well represented and shock position and strength are correctly estimated. However, influence of the tip leakage flow (TLF) and its interaction with the shock are slightly overestimated by numerical simulations. At DP, the angle of the TLF in RANS is inclined further in circumferential direction. At PP, the influence downstream of the shock is much weaker in the experiment, indicating stronger mixing in agreement with the interpretation of the radial profiles in Fig. 5.

Figure 7(b) shows the wall pressure field at 80% design speed. In contrast to Fig. 7(a) no shocks are observed as the rotor is operating subsonic at this speedline. Throttling the rotor from NC to NS results in an increased static-to-total pressure ratio within the whole passage and inclining tip leakage flow. At near choke condition, the contours indicate flow separation at 70% chord, consistently estimated by RANS. Agreement with numerical simulations is even better than at design speed, local structures and absolute values are well estimated by the employed RANS simulations. Merely the low static pressure region on the blade suction side close to the LE is numerically under-estimated. This effect can be associated to the increased tip clearance of the real geometry, discussed in the next section.

In conclusion, deviations between numerical simulations and experiments are localized in the tip region and associated to the numerical setup. The static pressure field at the casing is well estimated by the used numererical simualtions but the mixing of the tip flow with the main passage flow remains challenging and will be subject to further research. Towards midspan and the hub numerical simulations are accurate for all investigated operating points. Specific focus must be laid on the influence of turbulence modeling and transition to assess the scalability of the obtained results to full size applications.

3 System symmetry, blade-to-blade variation and deviation from design

In this section the influence of deviations of the experimentally investigated rotor from the numerical design is investigated. Simulation of composite layups is still challenging today and systematic errors cannot be avoided. The primary reason for deviations from design is the difference between the manufac-

turing process and the used FEM model. The ACT module implemented in the commercial ANSYS Workbench 18.2 toolbox was used for all static and modal calculations and requires the assumption of layers perfectly parallel to the respective profile centerline, as described in [7]. In the fabricated geometry, layers follow the molded surfaces of the blade and meet at the centerline.

The second reason for deviations are fabrication tolerances. Molding, pressing, curing and demolding procedures have non-negligible influence on surface quality and geometry. Tip geometry is manufactured conventionally after demolding and causes further inaccuracy. Using a clearly defined procedure, 48 blades have been produced and analyzed, yielding a quality that exceeded expectations but still comprised blade-to-blade variations. A detailed report on fabrication and static mode analysis is published under https://cordis.europa.eu/project/id/864719/results. The most similar 16 blades in terms of eigenfrequencies have been selected for the reference configuration based on cold measurements discussed in [22]. As will be shown in the next sections, blade-to-blade variation of tip clearance and stagger angle is not negligible.

3.1 Tip Clearance

Figure 8 presents measured tip clearance during an acceleration of the rotor from minimum to 102% design speed. The shown curves represent the averaged value of all blades at 11% (LE), 62% (MC) and 88% (TE) axial chord (solid lines) and are compared to the tip clearance used to simulate the rotor (symbols) in the design phase (FEM and RANS).

In Fig. 8(a) the reduction of tip clearance with rotational speed is presented. The experimental consumption (i.e. the reduction) of tip clearance from 50% to 100% design speed at mid-chord is about 0.18 mm hence approximately 15% of the cold tip clearance at this position. At 11% axial chord this consumption is slightly lower, at 88% higher due to blade untwist. In the FEM simulation this evolution is well estimated but with a nearly constant offset for all axial positions. For design speed conditions, measured tip clearance at 11% chord is approximately 0.10 mm higher than numerically computed, while it is 0.10 mm and 0.12 mm smaller at 62% and 88% axial chord respectively.

Fig. 8(b) visualizes the blade tip clearance as a function of axial chord. Whereas a linear clearance evolution was designed and used for numerical simulations the real geometry is slightly curved, requiring a polynomial fit. For both presented speedlines the tip clearance reaches a maximum at the LE in experiments. Downstream of about 35% axial chord, measured tip clearance is smaller than numerically estimated but differences between both shapes are smaller than in the LE region. Measurements of the cold geometry indicate that the average clearance deviation is attributed to blades and casing by equal parts, which have both been manufactured within a local tolerance of the order of 0.1 mm. Detailed values are provided in Tab. 3 in the appendix.

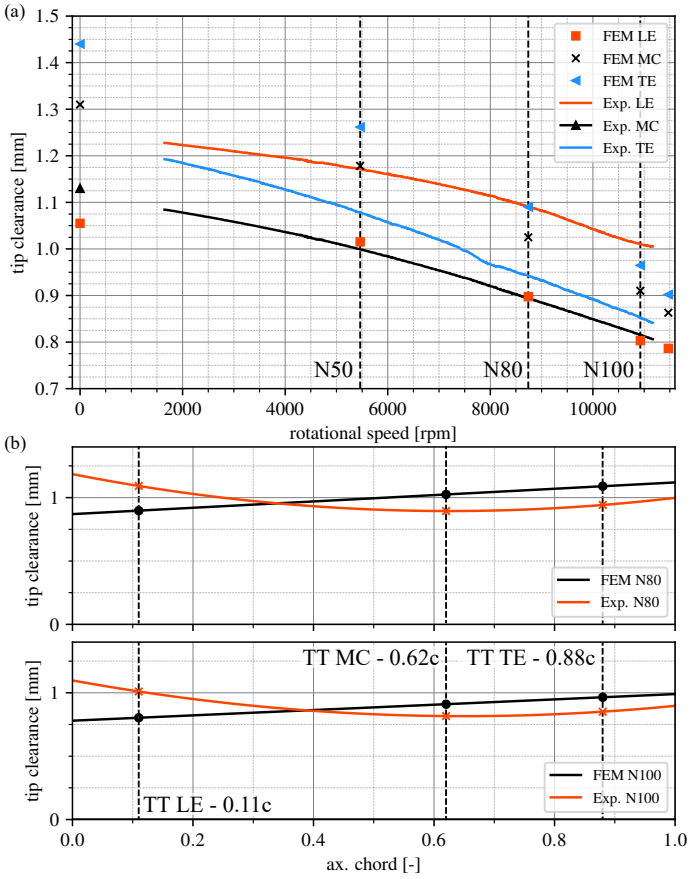

FIGURE 8: Tip clearance at different axial positions as a function of rotational speed at design conditions

While Fig. 8 shows only the measured average tip clearance of all blades, Fig. 9 presents the individual clearance of each blade for 80% and 100% design speed for design operating conditions (DP). As before, the tip clearance for three different axial positions is analyzed.

The tip clearance at 80% design speed varies about 0.17 mm, 0.14 mm and 0.21 mm from peak-to-peak at 11%, 62% and 88% axial chord respectively. At design speed the inter-blade variation is with 0.17 mm at 11% axial chord identical and with 0.12 mm at 62% axial chord slightly smaller. At 88% axial chord i.e. close to the blade's trailing edge the difference between minimum and maximum tip clearance increases to 0.26 mm.

The visualization in Fig. 9 reveals a distinct pattern in blade tip shape, which changes only marginally from part to design speed. This indicates that the pattern is caused by fabrication tolerances and not significantly influenced by operating conditions as rotational speed and massflow rate. This measured variation exceeds by far the inaccuracy of the molded profile shapes. We consider to readjust individual blades for future measurement campaigns.

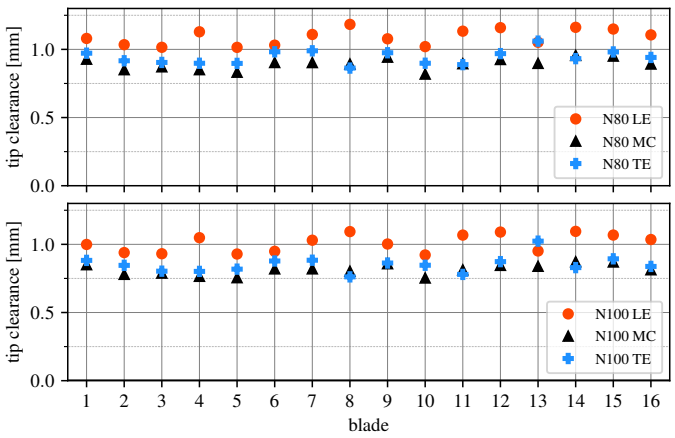

FIGURE 9: Blade-to-blade variation: tip clearance at different axial positions at 80% (top) and design speed (bottom) at respective design point conditions

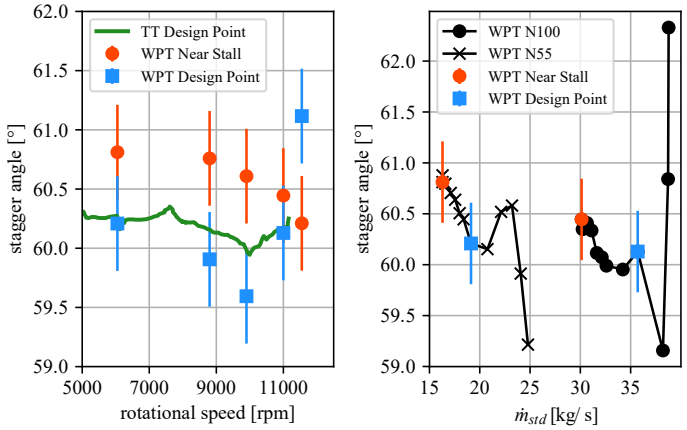

FIGURE 10: Rotor blade stagger angle as a function of rotational speed and massflow

Figure 9 highlights a few blades, for example blade 8 and 13, whose shape differs stronger from the averaged shape presented in Fig. 8(b). These deviations influence the flow field at the rotor blade tip as discussed in the following section. Summarized, the manufactured tip clearance deviates from the design intention and blade-to-blade variations are not negligible. Prediction of the evolution of tip clearance with speed by FEM is yet accurate. The presented results of the real tip clearance can be directly used by the community to adapt future simulations.

3.2 Stagger Angle

A second parameter which has a strong impact on rotor tip aerodynamics is the blade stagger angle. For the measurements presented in this paper, the stagger angle is defined through the intersection of the blade tip with the leading and trailing-edge tip-timing positions (TT LE and TT TE i.e. 11% and 88% axial chord respectively). FEM calculations (as shared with the open-test-case geometry [7]) indicate a stagger angle of 60.3° at 55% speed, slightly opening to 60° at 100% speed.

Figure 10 presents the experimental stagger which is determined based on gradient detection in the signals of the axial WPT array above the blade tip from 11% to 88% axial chord (compare Fig. 7) [31]. The presented data has been ensemble averaged over 200 revolutions and all blades, error bars represent maximum deviations. The data is compared to the measurement with the tip-timing system, which only provides average values per revolution for design conditions (DP).

The evolution over rotational speed shown in Fig. 10(a) reveals a strong dependence of the blade stagger angle from the operating conditions. Increasing the rotation speed to 10000 rpm (≈ 90% design speed) leads to a continuous decrease of stagger angle at design and peak efficiency conditions. At transonic speeds, this trend is inverted. For near stall conditions, the stagger angle decreases over the whole speed range by about 0.5°.

Figure 10(b) allows a detailed analysis of the influence of massflow rate on blade stagger. For both presented speedlines, blade stagger angle decreases as massflow rate is increased from NS to intermediate massflows. For intermediate massflow rates close to design point blade stagger angle reaches a plateau. Further increasing the massflow rate results in a behavior depending on the speedline. At subsonic speed (N55) the stagger angle decreases whereas at transonic speed (N100) the change of shock topology from design point towards near choke leads to a sharp increase of stagger angle to up to 62.3°. This phenomenon clearly explains the massflow discrepancy observed near choke in Fig. 4 towards the RANS simulations, which are all considering the average stagger angle of 60° calculated by FEM for peak efficiency conditions. The global trend of decreasing stagger angle from near stall to near choke conditions is related to coupling of numerous phenomena such as shock position and strength, radial mass distribution and tip blockage.

To investigate blade-to-blade variations and the influence on rotor tip aerodynamics, Fig. 11 presents the ensemble averaged static wall pressure field (averaged over 200 rotor revolutions to remove temporal fluctuation) for one rotor revolution at three different operating conditions. From the static pressure field shown on the left-hand side for each operating point, blade-to-blade variations are only visible for peak efficiency. For example shock strength and the interaction between shock and tip leakage vortex is higher for blade 10 and 13 compared to all other blades. To highlight differences, the averaged passage wall pressure is subtracted from the individual blade pressure field, yielding the graphs presented on the right-hand side of each operating point. Blade-to-blade variations are emphasized and also visible for near stall and near choke operating conditions. Deviations from the average passage are observed in the blade LE and shock re-

gion as well as in the interaction zone of TLF and shock due to the high sensitivity of these phenomena towards slight changes in blade geometry. However, deviations from the average passage at near stall and near choke are small compared to those at peak efficiency. At PE the blade pairs 9/10 and 12/13 develop strong variations in the shock region, caused by differences in shock position and strength, but also in the supersonic expansion zone near the leading edge

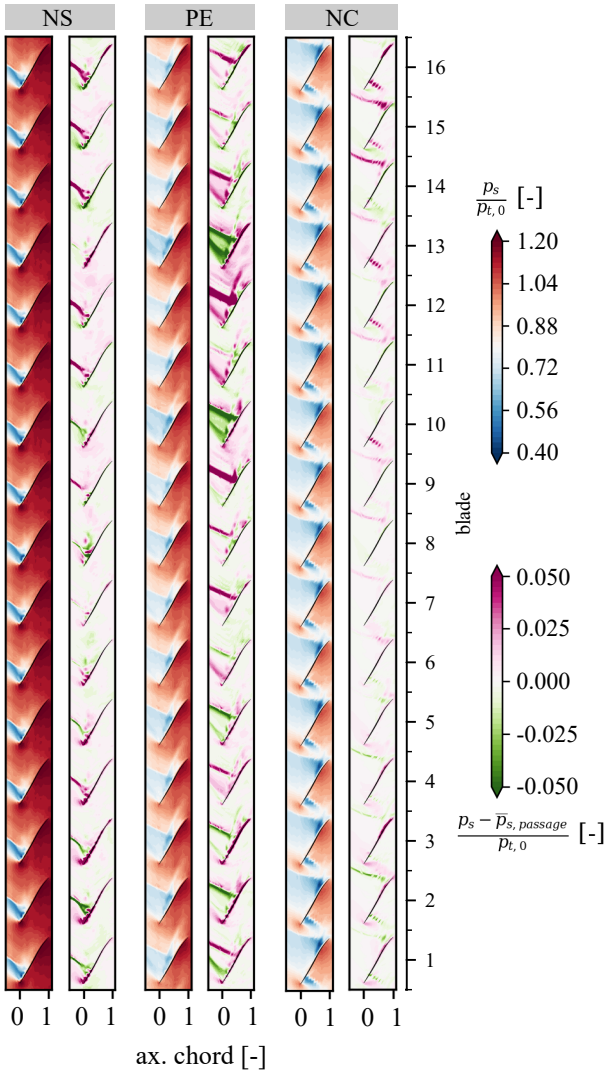

FIGURE 11: blade-to-blade variation: ensemble averaged flow field and deviation from average passage flow field at three operating conditions at design speed: near choke (right, 38.6 kg/s), peak efficiency (center, 36.8 kg/s), near stall (left, 30.5 kg/s), see Fig. 4.

To quantify these observations and investigate correlations, Fig. 12 shows average values and temporal fluctuations of stagger angle and shock position for each blade. The shock position is derived from chordwise pressure gradients in the WPT measurements and the distance to the blade leading edge related to the chord length (details in [31]). Three operating conditions are shown, near choke, peak efficiency and near stall.

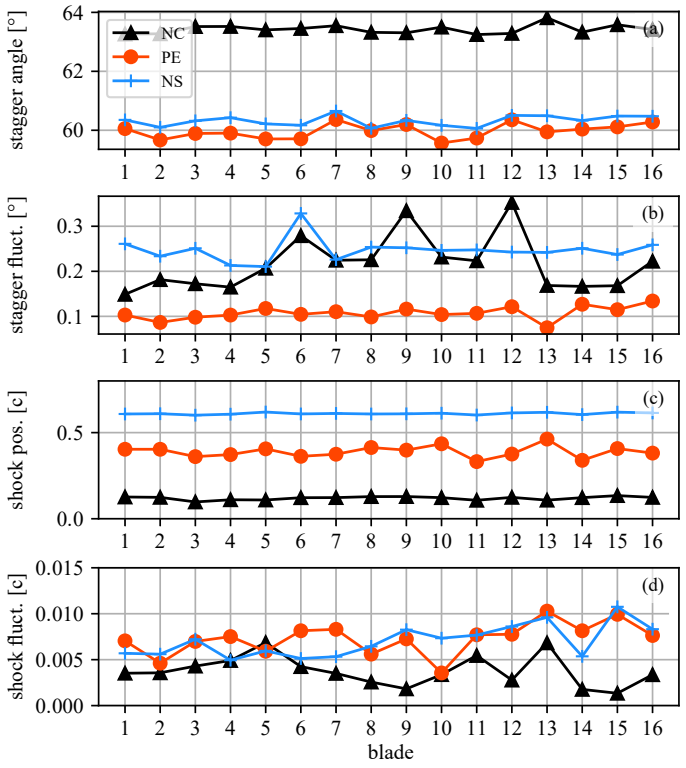

FIGURE 12: Blade-to-blade variation: average value and temporal fluctuation of stagger angle and shock position at three operating conditions at design speed: near choke (black, 38.6 g/s), peak efficiency (orange, 36.8 kg/s), near stall (blue, 30.5 kg/s), see Fig. 4

The illustration of the stagger angle Fig. 12(a) shows the highest stagger angle at near choke condition, while the two other operating points are at comparable level. Blade-to-blade variation is significant. The observed pattern is homogeneous for peak efficiency and near stall but changes near choke. Comparison with stagger fluctuations (temporal standard deviation) Fig. 12(b) shows that peak efficiency is the most stable condition with fluctuations of 0.1°, near choke and near stall presenting fluctuations of the order of 0.2°-0.3° with more prominent patterns. Analysis of the shock position reveals that a strong blade-to-blade variation of the average position Fig. 12(c) is observed at peak

efficiency whereas temporal fluctuations (d) are low (below 1% chord). From this data it is not possible to derive a clear correlation between stagger angle and shock.

The variation of tip clearance is correlated at peak efficiency condition. Blade 10 and 13 were standing out in Fig. 9 with low leading edge clearance, which affects the trailing shock. This is observed in Fig. 12(c) where at peak efficiency the shocks of blade 11 and 14 are less detached than the average, resulting in high asymmetry levels in Fig. 11. The opposite is observed for blade 12 which has a high leading edge clearance, producing a far detached shock ahead of blade 13. For this blade, the lowest stagger fluctuations are observed. At near stall and near choke condition this correlation is not observed.

The previously discussed values are illustrated in Fig. 13 over massflow for design speed. A non-linear evolution of the average stagger angle (a) is observed between near choke and design point, due to the change of shock topology. Maximum blade-to-blade variation of the stagger angle (b) is between 0.5 and 1°, mostly constant over the massflow range, temporal fluctuations are continuously rising from DP to an order of 0.2° at near stall condition.

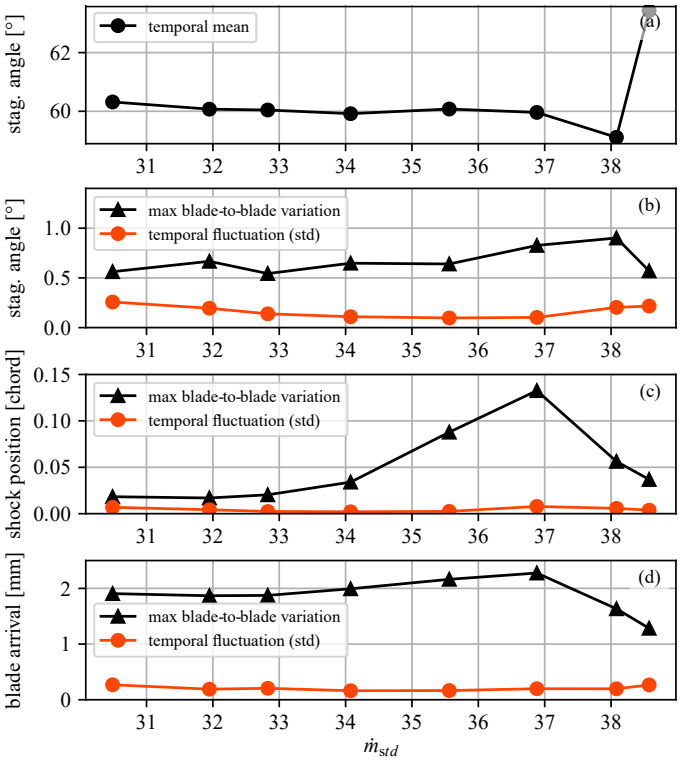

FIGURE 13: Maximum blade-to-blade variation (black) and temporal fluctuation (red) of stagger angle, shock position and blade arrival as function of massflow at design speed

As already observed in Fig. 11, the shock position is most unsymmetric at peak efficiency condition, varying from blade to blade by up to 13% of chord. These graphs emphasize that blade-to-blade variations are more severe than pure unsteadiness for this configuration. This must be investigated in the future regarding the theories on alternate passage divergence such as presented by [3, 2].

The last graph in Fig. 13(d) presents the variation of the blade arrival, i.e. the angular position of the tip with respect to the mean value. Here an unexpected high variation with a maximum of 2 mm is observed at peak efficiency conditions. This value is of the same order of magnitude as the blade thickness at the tip and highly relevant for tonal noise and aeroelastic interactions. Again, temporal fluctuations are low, hence a stable but asymmetric pattern is observed.

The entirety of these observations was not expected during design. Tip clearance and stagger asymmetry and their unsteadiness as well as the evolution with speed and throttling conditions are partly counter-intuitive and pave the ground for future research. The applied methods with detailed and combined multi-physical instrumentation have proven necessary to resolve these phenomena.

Summarizing this section, the variation of stagger angle is not negligible, and blade-to-blade variations are significant. The average angle is well aligned with the design intention and working line simulations are accurate. The significant change of average stagger angle towards choke conditions is highly relevant and must be considered in future work. Same as for the real tip clearance measurements, the dimensional data presented here and in the appendix can be used by the community. A variety of simulations have already been conducted by international institutes using different methods with the theoretical design and are presented in the appendix.

Conclusion

The open-test-case fan ECL5/CATANA has been experimentally investigated with multi-physical instrumentation. The provided dataset comprises measurements of aerodynamic stage performance, radial profiles and time resolved measurements of tip-clearance, blade stagger angle and shock positions. Together with the already published geometry data of the composite fan design this dataset represents a complete benchmark for modern fan architectures.

The experimental results of the reference campaign have shown that the general aerodynamic performance of the configuration was well estimated by wall-resolved RANS simulations of ECL and international institutes (see Fig. 14 in appendix). For all subsonic and transonic speedlines, the stage pressure ratio was slightly higher than in RANS simulations when approaching choke condition, which could be associated to an over-estimation of OGV-corner separations. Towards stall

measured pressure characteristics coincide with numerical estimations, same as peak efficiency which is at the same level as in CFD (92% at design speed), but observed at slightly higher massflows.

Average wall pressure contours coincide well between experiments and numerics and confirm far detached shocks at design conditions, which is in clear contrast to existing HBR-configurations with higher relative speeds.

Through extensive instrumentation additional information on the running geometry could be derived, which revealed differences to the FEM calculations and can be used for more accurate CFD simulations. While the average mid-chord tip clearance evolves as estimated over the speed range, the clearance at leading edge is higher than designed. Same applies to the stagger-angle, which opens by about 0.8° from 50 to 100% of design speed. At all speedlines, significant change of the average stagger angle is measured between choke and design conditions, which has not been taken into account in previous CFD simulations but can be implemented with the provided measurements.

Moderate blade-to-blade variations are observed and increase with rotation speed. Both tip-clearance and stagger-angle reveal patterns that affect the local aerodynamic fields. A circumferential stagger-asymmetry is observed at transonic conditions, that is most severe at design conditions and decreases towards choke or stall. Traveling alternate passage divergence or periodic changes of stagger patterns have not been observed, merely correlations between shock position and leading edge tip clearance. This observation is of relevance for future designs as it contrasts literature on recent industrial designs.

The investigation of operability has revealed significant non-synchronous vibration at all subsonic speedlines (55% - 90%) at comparable throttle conditions, leading to experiment abortion due to critical vibration amplitudes before onset of stall. At transonic conditions (100% and 105%), rotating stall is observed without any modal or structural precursors, as discussed in a dedicated publication [22]. The overall stability limit is continuous and not interrupted by specific flutter-bites, which might be a step-change compared to existing high-speed configurations. The presented reference experiment is highly promising for future research with the configuration, as both performance and operability are close to design and can be used as a reliable benchmark for numerical method development. The manufactured fan stage has proven robust and safely operational. Used instrumentation is suitable to investigate the local flow field, vibration patterns and amplitudes as well as blade-to-blade variations which will be relevant for upcoming experiments on intentional structural and geometric mistuning, acoustic intake variations and inlet distortions. The data presented in this paper comprises all relevant information to set-up and validate steady simulations at subsonic and transonic speeds using measured running geometry and even blade-to-blade variations. Associated raw data will be made available to the research community.

Acknowledgments

The results presented in this paper rely on the contributions of a large research group and the authors gratefully acknowledge the excellent collaboration and support over the past five years. The authors particularly thank Pavel Teboul, Cedric Desbois, Sebastien Goguey, Gilbert Halter, Lionel Pierrard, Laurent Pouilloux, Edouard Salze of LMFA, Kevin Billon and Claude Gibert of LTDS for their support and contributions to the experiments.

The authors recall that the development of the fan was conducted within the thesis of Valdo Pages and supervised by Stephane Aubert, Pascal Ferrand, Pierre Duquesne from LMFA and Laurent Blanc from LTDS. The final design was developed in close collaboration with Safran Aircraft Engines, and the authors particularly acknowledge the help of Laurent Jablonski. We are grateful for the continuous collaboration and financial support of SAFRAN Aircraft Engines since the beginning of this project and specifically for the present measurement campaign, for which the test module MARLYSA was provided by SAFRAN.

For the tip-timing measurements we received extensive support of Gerhard Ziller, Marco Hermann and Simon Kytzia of MTU Aero Engines.

The presented research was financed through the European Union's Clean Sky 2 Joint Undertaking (JU) under grant agreement N864719, CATANA. The JU receives support from the European Union's Horizon 2020 research and innovation program and the Clean Sky 2 JU members other than the Union. The paper reflects only the author's view and the JU is not responsible for any use that may be made of the information it contains. Assessment of the test facility was enabled through financial supports of Agence Nationale de la Recherche (ANR, Project d'EqupEx PHARE) and Conseil pour la Recherche Aeronautique Civile (CORAC - Programme CUMIN). Buildings and infrastructure were supported by ECL, instrumentation supported by Institut Carnot (INGENIERIE@LYON - Project MERIT) and SAFRAN Aircraft Engines.

REFERENCES

[1] Peters, A., Spakovszky, Z. S., Lord, W. K. and Rose, B. "Ultra-Short Nacelles for Low Fan Pressure Ratio Propulsors." *Proc. ASME Turbo, GT2014-26369*. 2014. DOI 10.1115/GT2014-26369.

[2] Wilson, Mark J., Imregun, Mehmet and Sayma, Abdulnaser I. "The Effect of Stagger Variability in Gas Turbine Fan Assemblies." *J. Turbomach.* Vol. 129 No. 2 (2006): pp. 404–411. DOI 10.1115/1.2437776.

[3] Lu, Yaozhi, Lad, Bharat, Green, Jeff, Stapelfeldt, Sina and Vahdati, Mehdi. "Effect of geometry variability on transonic fan blade untwist." *Int. J. Turbomach., Propulsion and Power* Vol. 4 No. 3 (2019): p. 24. DOI 10.3390/ijtpp4030024.

[4] Pages, V., Duquesne, P., Aubert, S., Blanc, L., Ferrand, P., Ottavy, X. and Brandstetter, C. "UHBR Open-Test-Case Fan ECL5/CATANA." *Int. J. Turbomach., Propulsion and Power* Vol. 7 No. 2 (2022): p. 17. DOI 10.3390/ijtpp7020017.

[5] Eggers, T., Friedrichs, J., Goessling, J., Seume, J. R., Natale, N., Flüh, J.P. and Paletta, N. "Composite UHBR Fan for Forced Response and Flutter Investigations." *Proc. ASME Turbo, GT2021-58941*. 2021. DOI 10.1115/GT2021-58941.

[6] Brandstetter, C., Pages, V., Duquesne, P., Ottavy, X., Ferrand, P., Aubert, S. and L., Blanc. "UHBR open-test-case fan ECL5/CATANA, Part 1 : Geometry and aerodynamic performance." *Proc. ETC14, ETC2021-626*. 2021. DOI https://hal.archives-ouvertes.fr/hal-03257374.

[7] Pages, V., Duquesne, P., Ottavy, X., Ferrand, P., Aubert, S., Blanc, L. and Brandstetter, C. "UHBR open-test-case fan ECL5/CATANA, Part 2 : Mechanical and aeroelastic stability analysis." *Proc. ETC14, ETC2021-625*. 2021. DOI https://hal.archives-ouvertes.fr/hal-03257377.

[8] Fiquet, A.-L., Ottavy, X. and Brandstetter, C. "UHBR Open-Test-Case Fan ECL5/CATANA: Non-linear analysis of non-synchronous blade vibration at part-speed condtions ." *ISUAAAT16, ISUAAAT16-064*. 2022. DOI https://hal.archives-ouvertes.fr/hal-03800486.

[9] Kielb, R. E., Barter, John W., Thomas, Jeffrey P. and Hall, Kenneth C. "Blade Excitation by Aerodynamic Instabilities: A Compressor Blade Study." *Proc. ASME Turbo*: pp. 399–406. 2003. DOI 10.1115/GT2003-38634.

[10] Brandstetter, C., Juengst, M. and Schiffer, H.-P. "Measurements of Radial Vortices, Spill Forward, and Vortex Breakdown in a Transonic Compressor." *J. Turbomach.* Vol. 140 No. 6 (2018): p. 061004. DOI 10.1115/1.4039053.

[11] Rodrigues, M., Soulat, L., Paoletti, B., Ottavy, X. and Brandstetter, C. "Aerodynamic investigation of a composite low-speed fan for UHBR Application." *J. Turbomach.* Vol. 143 No. 10 (2021): p. 101004. DOI 10.1115/1.4050671.

[12] Schneider, A., Paoletti, B., Ottavy, X. and Brandstetter, C. "Influence Of A Turbulence Control Screen On The Aerodynamic And Aeroelastic Behavior Of A Uhbr Fan." *Proc. ASME Turbo Expo 2022, GT2022-81961*. 2022.

[13] Stapelfeldt, S. and Brandstetter, C. "Non-synchronous vibration in axial compressors: Lock-in mechanism and semi-analytical model." *J. Sound and Vibration* Vol. 488 (2020): p. 115649. DOI 10.1016/j.jsv.2020.115649.

[14] Brandstetter, C. and Stapelfeldt, S. "Analysis of a linear model for non-synchronous vibrations near stall." *Int. J. Turbomach., Propulsion and Power* Vol. 6 No. 3 (2021): p. 26. DOI 10.3390/ijtpp6030026.

[15] Al-Am, Jean, Clair, Vincent, Giauque, Alexis and Boudet, J. "A Parametric Study on the LES Numerical Setup to Investigate Fan/OGV Broadband Noise." *International Journal of Turbomachinery, Propulsion and Power* Vol. 6 No. 2 (2021): p. 12. DOI 10.3390/ijtpp6020012.

[16] Al-Am, Jean, Clair, Vincent, Giauque, Alexis and Boudet, J. "Direct noise predictions of fan broadband noise using LES and analytical models." *28th AIAA/CEAS Aeroacoustics 2022 Conference*. 2022. DOI 10.2514/6.2022-2882.

[17] Tucker, Paul G. and Tyacke, James C. "Eddy resolving simulations in aerospace - Invited paper (Numerical Fluid 2014)." *Applied Mathematics and Computation* Vol. 272 (2016): pp. 582–592. DOI 10.1016/j.amc.2015.02.018.

[18] Bode, C., Przytarski, P., Leggett, J. and Sandberg, R. D. "Highly Resolved Large-Eddy Simulations of a Transonic Compressor Stage Midspan Section Part I: Effect of Inflow Disturbances." *Proc. ASME Turbo, GT2022-81673*. 2022. DOI 10.1115/GT2022-81673.

[19] Bode, C., Przytarski, P., Leggett, J. and Sandberg, R. D. "Highly Resolved Large-Eddy Simulations of a Transonic Compressor Stage Midspan Section Part II: Effect of Rotor-Stator Gap." *Proc. ASME Turbo, GT2022-82474*. 2022. DOI 10.1115/GT2022-82474.

[20] Brandstetter, C., Pages, V., Duquesne, P., Paoletti, B., Aubert, S. and Ottavy, X. "Project PHARE-2 : A High-Speed UHBR Fan Test Facility for a New Open-Test Case." *J. Turbomach.* Vol. 141 No. 10 (2019): p. 101004. DOI 10.1115/1.4043883.

[21] Lu, Y., Lad, B. and Vahdati, M. "Transonic Fan Blade Redesign Approach to Attenuate Nonsynchronous Vibration ." *J. Eng. Gas Turbines Power* Vol. 143 No. 7 (2021): p. 71007. DOI 10.1115/1.4050023.

[22] Fiquet, A.-L., Schneider, A., Paoletti, B., Ottavy, X. and Brandstetter, C. "Experiments on Tuned UHBR Open-Test-Case Fan ECL5/CATANA: Stability Limit." *Proc. ASME Turbo, GT2023-102537*. 2023.

[23] Cox, R. N. "Wall neighbourhood measurements in turbulent boundary layers using a hot wire anemometer." *Aeronaut. Res. Con., Report No. 19101*. 1957.

[24] Pages, Valdo. "Conception du fan UHBR ECL5 pour une analyse des mecanismes d'interactions multi-physiques a l'origine du flottement." *PhD thesis, Ecole Centrale de Lyon*. 2021. DOI http://www.theses.fr/2021LYSEC047/document.

[25] Cambier, L., Heib, S. and Plot, S. "The Onera elsA CFD software: input from research and feedback from industry." *Mechanics and Industry* Vol. 14 No. 3 (2013): pp. 159–174. DOI 10.1051/meca/2013056.

[26] Taylor, J. V. "Separated Flow Topology in Compressors." *J. Turbomach.* Vol. 141 No. 9 (2019): p. 091014. DOI 10.1115/1.4044132.

[27] Gbadebo, S. A., Cumpsty, N. A. and Hynes, T. P. "Three-dimensional separations in axial compressors ." *J. Turbomach.* Vol. 127 No. 2 (2005): pp. 331–339. DOI 10.1115/1.1811093.

[28] Liu, Y., Tang, Y., Scillitoe, A. D. and Tucker, P. G. "Modification of shear stress transport turbulence model using helicity for prediction corner separation flow in a linear compressor cascade ." *J. Turbomach.* Vol. 142 No. 2 (2020): p. 21004. DOI 10.1115/1.4045658.

[29] Denton, J. D. "Some limitations of turbomachinery CFD." *Proc. ASME Turbo, GT2012-22540*. 2010. DOI 10.1115/GT2010-22540.

[30] Fiquet, A.-L., Ottavy, X. and Brandstetter, C. "UHBR Open-Test-Case Fan ECL5/CATANA: Numerical Investigation Near The Stability Limit Including Aerodynamic Mistuning." *Proc. ASME Turbo Expo 2022, GT2022-77992*. 2022.

[31] Brandstetter, C., Kegalj, M., Wartzek, F., Heinichen, F. and Schiffer, H.-P. "Stereo PIV Measurement of Flow Structures underneath an Axial-Slot Casing Treatment on a One and a Half Stage Transonic Compressor." *Proc. 17th Int. Symposium on Applications of Laser and Imaging Techniques to Fluid Mechanics*. 2014. DOI 10.13140/RG.2.1.2175.1768.

[32] Moreau, Antoine. "A unified analytical approach for the acoustic conceptual design of fans of modern aero-engines." *PhD thesis, Technical University of Berlin and DLR internal report*. 2017.

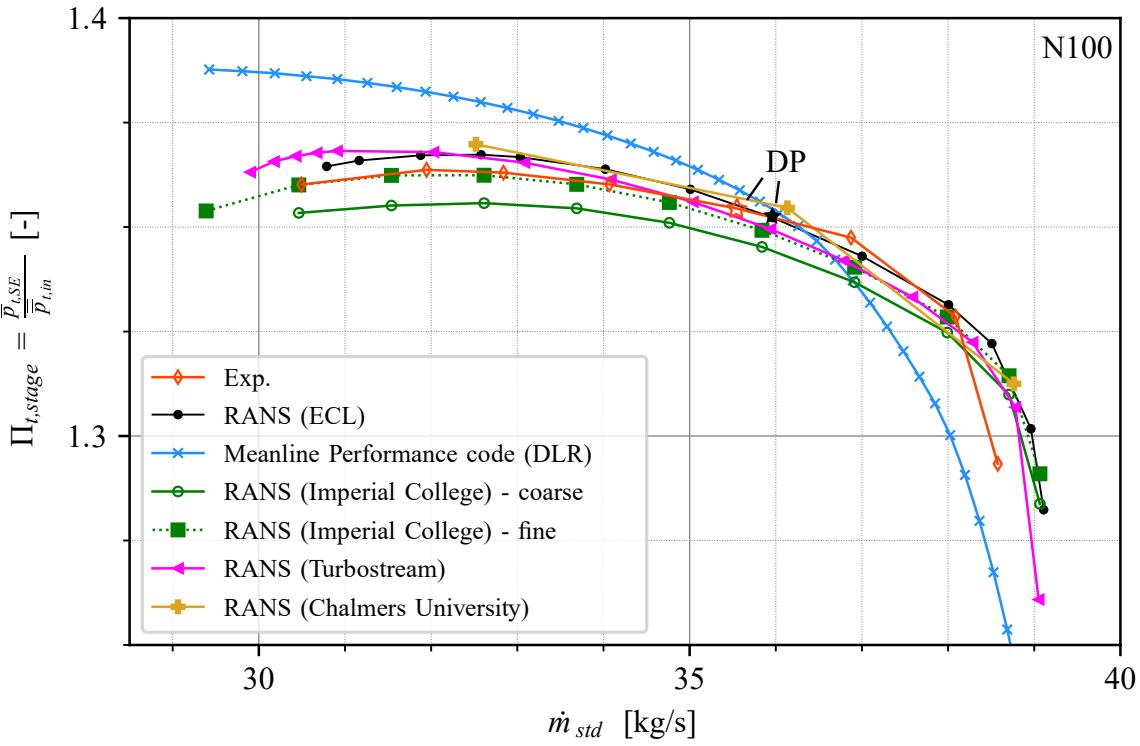

FIGURE 14: Fan stage total pressure ratio: comparison of experimental data and numerical results from research community

Appendix: Relevance for the research community

The design geometry for the fan stage has been introduced at the ETC conference in 2021 [6, 7]. Several international research institutes have been provided with the detailed geometry to follow different objectives. Three institutes have already performed simulations which are compared in the following. Imperial College (s.stapelfeldt@imperial.ac.uk, pierre.tharreau18@imperial.ac.uk) uses the unstructured URANS code AU3D and wall-modeling with the aim to perform coupled aeroelastic simulations (fine mesh with $1.7 \cdot 10^6$ cells, coarse $0.57 \cdot 10^6$ cells). Turbostream (tobias@turbostream-cfd.com, ewan@turbostream-cfd.com) aims for accurate unsteady simulations using wall-functions on a mesh with $3.1 \cdot 10^6$ cells in the Rotor and $0.94 \cdot 10^6$ in the Stator. Chalmers University of Technology (oliver.sjogren@chalmers.se) used ANSYS CFX, k-ω SST RANS with $5.4 \cdot 10^6$ cells in the rotor domain and $1.3 \cdot 10^6$ cells in the stator domain. The already discussed RANS setup of ECL (elsA) comprises $4.4 \cdot 10^6$ cells without wall functions. The engine acoustics department of DLR (antoine.moreau@dlr.de) uses a semi-empirical meanline performance code at 70% span within its fan noise prediction tool PropNoise (see [32] for details), dedicated to acoustic preliminary design.

Figure 14 compares the results for the total stage pressure ratio at 100% design speed.

RANS results from the fine mesh of Imperial College, Turbostream and Chalmers provide excellent overall agreement with the experimental data and are also close to the simulations of ECL. As the aim of the steady RANS simulations is not the accurate estimation of stall onset, differences are not discussed at this point. All numerical simulations estimate a comparable massflow at choke conditions, which is higher than in the experiment due to the changed stagger angle, discussed in previous sections. Results from the meanline approach of DLR coincide well with experiments at design conditions, also at not-shown part-speedlines. For throttled and unthrottled conditions the estimation deviates with a steeper characteristic than the experiment.

This comparison already highlights the relevance of the test case, providing validation data for institutes with different research objectives on aerodynamics, aeroelasticity and acoustics. State-of-the-art RANS simulations estimate closely the experimental results, which have proven a high repeatability and cross-validation with complementary instrumentation. Estimation inaccuracies can be addressed in the future using the extended information provided in this publication on running geometry and blade-to-blade variations.

TABLE 1: Nomenclature of operating points

	NC	PE	DP	PP	NS
% design speed	$\dot{m}_{std}$ [kg/s] / $\Pi_{t,stage}$ [-] / $\eta_{t,stage}$ [-]				
55	26.1 / 1.07 / 0.873	21.99 / 1.09 / 0.909	- / - / -	17.49 / 1.1 / 0.859	16.48 / 1.1 / 0.831
80	35.24 / 1.16 / 0.848	- / - / -	30.42 / 1.20 / 0.916	25.72 / 1.22 / 0.874	23.9 / 1.21 / 0.830
100	38.64 / 1.29 / 0.857	36.93 / 1.35 / 0.923	35.61 / 1.35 / 0.921	32.0 / 1.36 / 0.883	30.54 / 1.36 / 0.856

TABLE 2: Blade stagger angle

blade	stag. cold [°]	stag. N100 NC [°]	stag. N100 PE [°]	stag. N100 NS [°]
1	58.87	63.26	60.06	60.35
2	59.22	63.27	59.67	60.10
3	58.42	63.52	59.89	60.32
4	57.69	63.52	59.90	60.43
5	58.26	63.41	59.70	60.22
6	58.90	63.45	59.71	60.17
7	58.11	63.55	60.36	60.65
8	59.24	63.32	59.99	60.07
9	58.68	63.31	60.20	60.34
10	58.75	63.50	59.57	60.17
11	59.13	63.25	59.74	60.06
12	61.63	63.29	60.36	60.50
13	58.46	63.82	59.95	60.49
14	58.27	63.33	60.04	60.33
15	58.71	63.58	60.11	60.48
16	59.00	63.42	60.28	60.48

TABLE 3: Deviation from cold blade tip geometry from design from 3D scans and running tip clearance

	3D scan tip geometry			tip clearance N80 [mm]			tip clearance N100 [mm]		
blade	LE	MC	TE	LE	MC	TE	LE	MC	TE
1	-0.08	-0.08	-0.10	1.08	0.93	0.98	1.00	0.85	0.88
2	0.00	0.01	0.02	1.03	0.85	0.91	0.94	0.78	0.85
3	0.01	-0.08	-0.12	1.01	0.87	0.90	0.93	0.79	0.80
4	-0.09	-0.02	0.05	1.13	0.85	0.90	1.05	0.77	0.80
5	0.02	0.00	0.05	1.02	0.83	0.90	0.93	0.76	0.82
6	-0.10	-0.18	-0.24	1.03	0.90	0.98	0.95	0.82	0.88
7	-0.19	-0.18	-0.20	1.11	0.90	0.99	1.03	0.82	0.88
8	-0.22	-0.09	-0.01	1.18	0.89	0.86	1.09	0.80	0.76
9	-0.05	-0.21	-0.23	1.07	0.94	0.97	1.00	0.86	0.86
10	-0.01	0.01	0.00	1.02	0.82	0.90	0.92	0.75	0.85
11	-0.10	-0.11	0.06	1.13	0.89	0.89	1.07	0.81	0.78
12	-0.21	-0.15	-0.13	1.16	0.93	0.97	1.09	0.85	0.87
13	-0.06	0.01	0.00	1.05	0.90	1.07	0.95	0.84	1.02
14	-0.19	-0.16	-0.13	1.16	0.95	0.94	1.09	0.87	0.83
15	-0.16	-0.13	-0.08	1.14	0.95	0.99	1.07	0.87	0.89
16	-0.16	-0.10	0.02	1.11	0.89	0.94	1.04	0.81	0.84

TABLE 4: Design parameters

rotor diameter	508 mm
number of rotor blades	16
number of stator vanes	31
design speed	11000 rpm
design blade tip speed	288 m/s
design tip Mach number	1.02
design massflow rate	36.0 kg/s
design total pressure ratio	1.35
design isentropic efficiency	92.6%

The presented research was supported through Clean Sky 2 Joint Undertaking (JU), project CATANA under grant agreement N◦864719. The JU receives support from the European Union's Horizon 2020 research and innovation programme and the Clean Sky 2 JU members other than the Union. This publication reflects only the author's view and the JU is not responsible for any use that may be made of the information it contains.

catana.ec-lyon.fr
Christoph.brandstetter@ec-lyon.fr